Survival of the Fittest: Using a Genetic Evolutionary Algorithm to Design Better Fuel Cell Catalysts

Nathan Seth Froemming
Undergraduate Thesis in Physics
The University of Texas at Austin
August 19, 2008

Chapter 1

Survival of the Fittest: Using a Genetic Evolutionary Algorithm to Design Better Fuel Cell Catalysts

1.1 Introduction

Platinum-based fuel cells offer an attractive alternative to internal combustion engines as a future means of utilizing chemical energy, however, severe shortcomings of such technologies must be resolved if they are to become practical and widespread. Some of these difficulties include a disparity between the reaction rates at the anode and cathode, the short lifetime of electrodes in acidic environments, the energy loss due to a kinetic overpotential, and the high material cost and limited supply of Pt itself. Better catalysts need to be developed, yet the task of discovering cheaper, more effective platinum alternatives has proven to be extremely challenging. In this work, I investigate the catalytic properties of a large number of candidate replacement catalysts using a genetic algorithm (GA). Specifically, I apply the algorithm to bimetallic nanoparticles in which the core atom type differs from the shell atom type. In the algorithm, a chromosome that takes into account the identities of the core and shell represents each system, and each systems fitness is its ability to catalyze the oxygen reduction reaction (ORR), the so-called bottleneck of present fuel cell technologies. I evaluate the fitness of each system by using density functional theory (DFT) to calculate the electronic structure of the nanoparticle and, in some cases, to determine activation and reaction energies for the oxygen reduction reaction. At each step in the algorithm, the best catalysts in the population are selected for based on their fitness and bred by crossing their chromosomes, and the worst catalysts in the population are replaced with the offspring of the best catalysts. With time, subsequent generations evolve toward the best fitness, and I show how the energy of the electrons in the shell can be optimized for the oxygen reduction reaction by varying the core and shell metal types in the bimetallic nanoparticles. Promising platinum alternatives revealed by such a theoretically based search-and-screen approach may then be tested experimentally,

helping to alleviate the costly trial-and-error processes commonly used to optimize catalysts.

1.2 Possible Platinum Alternatives: Nanoparticles

One very attractive feature of nanoparticles is that they have much higher catalytic surface-area-to-volume ratios than bulk materials. Hence, the overall amount of electrode material required in platinum fuel cells could be dramatically reduced if reactive nanoparticle replacements were discovered, helping to reduce the overall cost of platinum-based fuel cells. Moreover, experiments have shown that the different electronic and geometric properties of nanoparticles can lead to dramaticaly different reactivities compared to bulk counterparts. An example of this phenomenon is shown in Figure 1.1, in which the reaction $CO+\frac{1}{2}O_2 \rightarrow CO_2$ on gold nanoparticles is monitored as a function of nanoparticle size. Curiously, gold nanoparticles approximately 2-5 nm in diameter are most active for this reaction, whereas larger nanoparticles are not; in the limit of large nanoparticle size, i.e. bulk gold, the reaction has completely ceased.

In this work, I'll be investigating small metal nanoparticles (both pure and core/shell-types) using a genetic algorithm in an attempt to see if I can optimize their reactivity for the reactions that occur in hydrogen fuel cells. The general structures of these nanoparticles are shown in Figure 1.2. Interestingly, a scientist at the University of Texas at Austin, Dr. Richard M. Crooks, has developed a clever way of very precisely controlling the synthesis of both pure and core/shell type nanoparticles called *dendrimer encapsulation* [2]. In this method a small, highly fragmented organic molecule (the dendrimer) serves as a template upon which the nanoparticles are built up via sequential reduction of metal cations in solution.

1.3 Genetic Algorithms

1.3.1 Overview

Searching for effective platinum alternatives has proven to be an incredibly difficult problem, mainly due to the phenomenal combinatorial burden associated with investigating such a large number of candidate catalysts experimentally, not to mention the incredible complexity of the solution space. This notion is shown in Figure 1.3. Even though the task of discovering cheaper, more effective platinum alternatives is seemingly intractable, there is hope: the genetic algorithm. Genetic algorithms have been proven to be a robust means of searching complicated solutions spaces. They work by randomly sampling the *entire* population of points in the solution space, not just a single region of solution space as with other methods (e.g. ones that involve calculus). The randomized searches of GAs, however, do not necessarily imply *directionless* searches, because of the predefined "fitness function." Even though a GA might pick unfit points in the solution space, it will discriminate against these unfit points using the fitness function. The GA then only allows the fit solutions to "breed", i.e. combine or mix with other fit solutions in an effort to project to new, possibly even more fit points in the solution space.

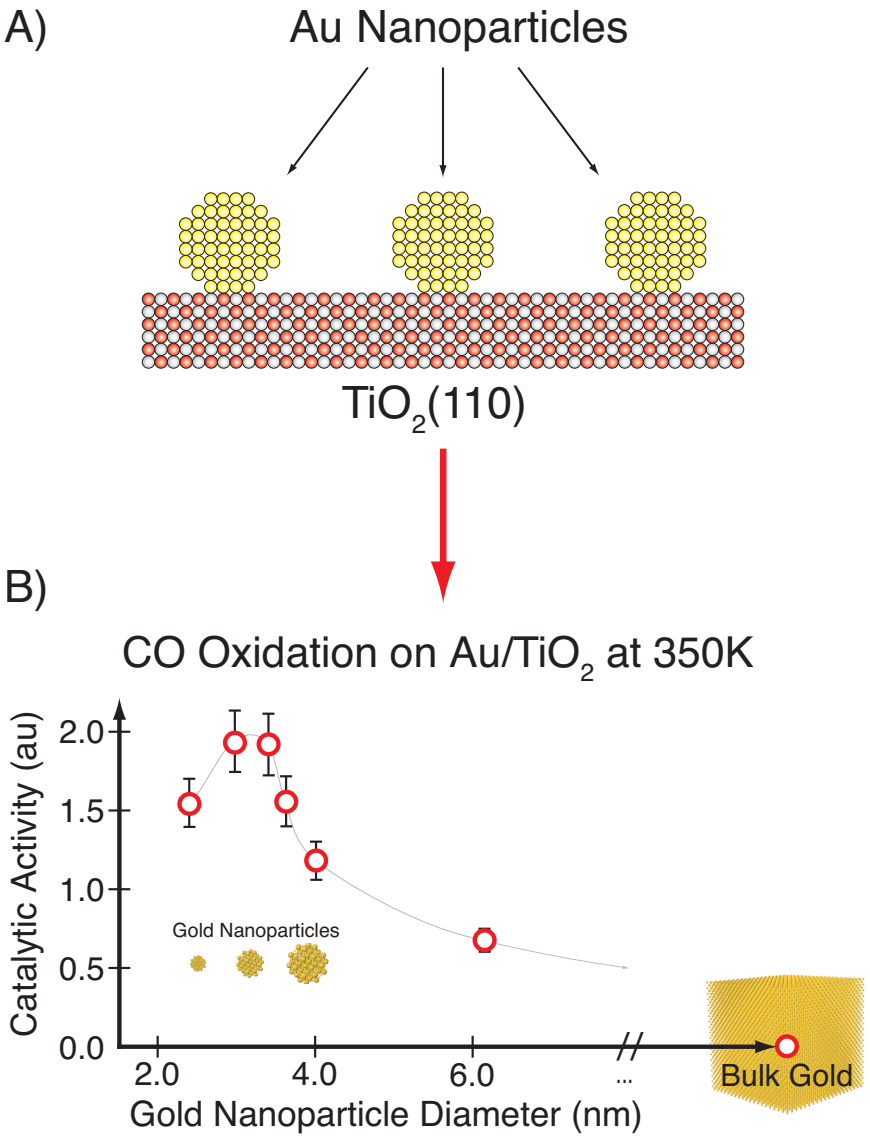

Figure 1.1: CO oxidation on gold nanoparticles at 350 K as measured by Goodman *et al.*[1]. (A) Gold nanoparticles are deposited onto a clean surface of $TiO_2(110)$, and (B) the reaction $CO + \frac{1}{2}O_2 \rightarrow CO_2$ is monitored as a function of nanoparticle size. CO oxidation proceeds most rapidly for gold nanoparticles approximately 2-5 nm in diameter. As the nanoparticles get larger, the rate of the reaction decreases dramatically. In the limit of large nanoparticle size, i.e. bulk gold, the reaction has completely ceased.

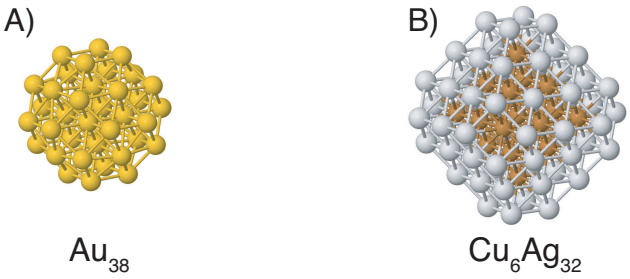

Figure 1.2: Examples of pure and core/shell type nanoparticles. (A) 38-atom pure gold nanoparticle. (B) 79-atom core/shell copper/silver nanoparticle.

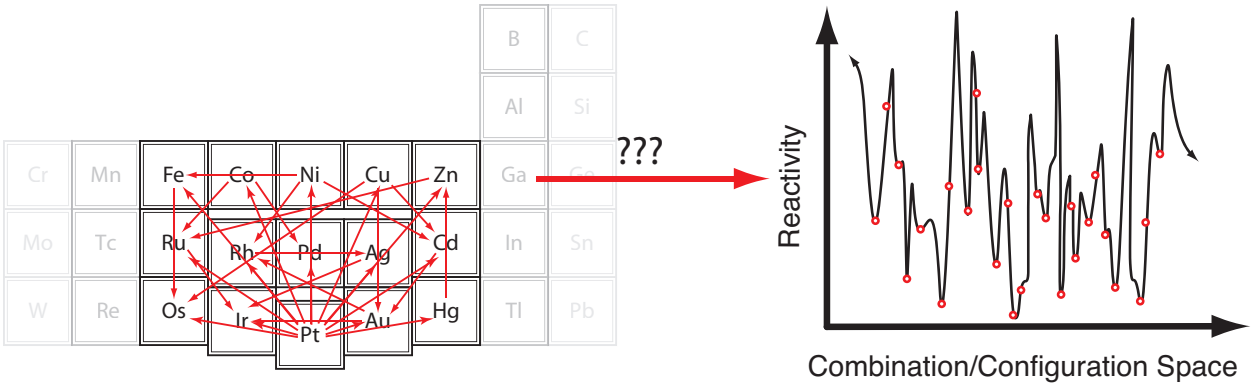

Figure 1.3: One of the major difficulties of searching for Pt alternatives is the phenomenal combinatorial burden associated with investigating such a large number of candidate replacement catalysts. My attempt to capture the scope of this problem is shown at the left, in which I only focus on a small region of the periodic table for clarity. Other major difficulties are that the solution space is incredibly complex (it contains all nanoparticle sizes, all different metal combinations, all different metal proportions, etc.) and undoubtedly discontinuous (atomic numbers are integers and do not increase continuously). My attempt to capture the scope of *this* problem is shown at the right.

1.3.2 Definition of the Fitness Function

We now turn to the issue of defining our fitness function. We already know that platinum is the best catalyst for the reactions that occur in hydrogen-based fuel cells, so why not try to emulate platinum? Since the valence electrons are responsible for determining chemical reactivity, we will attempt to mimic the electronic structure of the valence electrons of platinum, i.e. the *d-band electrons*. We will use density functional theory to calculate the electronic structure of a large number of candidate nanoparticle replacement catalysts (without actually having to make them!) and compare their electronic structure to that of the Pt(111) surface, i.e. the catalytic surface of a platinum electrode. Along these lines, we will only be looking at the d-band electrons in the *shell* of any candidate nanoparticle replacement catalyst that arises, i.e. the catalytic surface of the nanoparticle. The closer the electronic structure of the shell of the nanoparticle to that of Pt(111), the more "fit" that particular nanoparticle will be; the farther the electronic structure of the shell of the nanoparticle from Pt(111), the less "fit" that particular nanoparticle will be. These ideas lead us directly to our fitness function. The following equation will be used to assess the fitness of any given candidate replacement nanoparticle catalyst:

$$\mathrm{F} \equiv \left|\Delta\overline{\mathrm{E}}_{\text{d-band}}\right| \ . \tag{1.1}$$

Equation (1.1) states that the magnitude of the difference of the average energy of the d-bands of Pt(111) and the shell of any candidate nanoparticle in question will be computed, resulting in a number, called the *fitness number*, which will subsequently be used to rank the nanoparticles. The smaller the value of F, the closer the electronic structure of the shell of that particular nanoparticle from Pt(111), and the better the rank will be; the larger the value of F, the farther the electronic structure of the shell of that particular nanoparticle from Pt(111), and the worse the rank will be. The idea is that once we have looked at a few nanoparticles, we will "breed" only the most fit nanoparticles by mixing their metal types in an effort to project to new nanoparticles that possibly have electronic structures *even closer* to that of Pt(111). The details of this process are outlined in the next subsection.

1.3.3 Application of the Genetic Algorithm to Nanoparticles

To date, my research has consisted of running two genetic algorithms, one with small 38-atom core/shell nanoparticles and the other with larger, more realistic 79-atom core/shell nanoparticles like the ones shown in Figure 1.2. An overview of the application of the genetic algorithm to nanoparticles is shown in Figure 1.4. Although only the smaller 38-atom nanoparticles are shown in this figure, the genetic algorithm for the larger nanoparticles is very similar.

Step one consists of randomly generating an initial population of core/shell nanoparticles. Only metals from the d-block were investigated. It should be noted that pure nanoparticles are allowed if the same core and shell metal types are randomly chosen for a given nanoparticle (true at all points in the algorithms). The generation size remains fixed throughout the genetic algorithm at 20

nanoparticles. In step two, the structure of each nanoparticle in the generation is first minimized using density functional theory, then the average energy of the d-band electrons in the shell of each nanoparticle is calculated (this is by far the most time consuming step in the algorithm). In step three, the nanoparticles are ranked using the fitness function defined in Equation (1.1). Finally, in step four the nanoparticles are randomly bred based on their rank. The breeding probability was arbitrarily chosen to decay exponentially with rank number such that the higher-ranked nanoparticles had a greater chance of contributing to the next generation in the breeding process. Also shown in step four is the actual breeding process itself, in which the chromosomes of two randomly selected nanoparticles are bred by crossing their chromosomes. Each nanoparticle chromosome contained two pieces of information: the identity of the core and shell metal types. Each time a generation was bred, the top half of the generation was kept and the bottom half of the generation was replaced with the offspring of the most fit nanoparticles. After the next generation was formed, the algorithm then proceeded back to step number two, and the process outlined above was repeated. In this way, the generations continually evolved toward the best fitness. The mutations that were allowed in the genetic algorithms are shown in Figure 1.5. Each of these mutation types occurred with a probability of 10%. Mutations are very important in genetic algorithms because they allow the algorithm to become "unstuck" if it converges upon a local region of solution space.

1.4 Preliminary Results

1.4.1 Rapid Convergence and Hot Spots in Reactivity

The genetic algorithm involving the larger 79-atom nanoparticles is presently unfinished, and so I will mostly be discussing the results of the smaller 38-atom nanoparticle GA throughout the remainder of the text. As shown in Figure 1.6, the convergence of the generations toward the optimal fitness occurred rather rapidly – the GA had essentially converged after 5-6 generations. The nanoparticles at the endpoint of the GA should have shell electronic structures that are very similar to that of Pt(111), and hence might be worth investigating experimentally. Some of these possible "hot spots" in reactivity are shown in Figure 1.7.

1.4.2 Nanoparticle Reactivity for the Oxygen Reduction Reaction

We have shown in §1.4.1 that we can easily get the genetic algorithm to converge to optimal fitness, however, we must remember that the reaction we actually care about is the oxygen reduction reaction, the so-called bottleneck of present fuel cell technologies. This reaction occurs at the fuel cell cathode, the half-cell reaction for which is written as

$$\tfrac{1}{2}\mathrm{O}_2 + 2\mathrm{e}^- \rightarrow \mathrm{O}^{2-}. \tag{1.2}$$

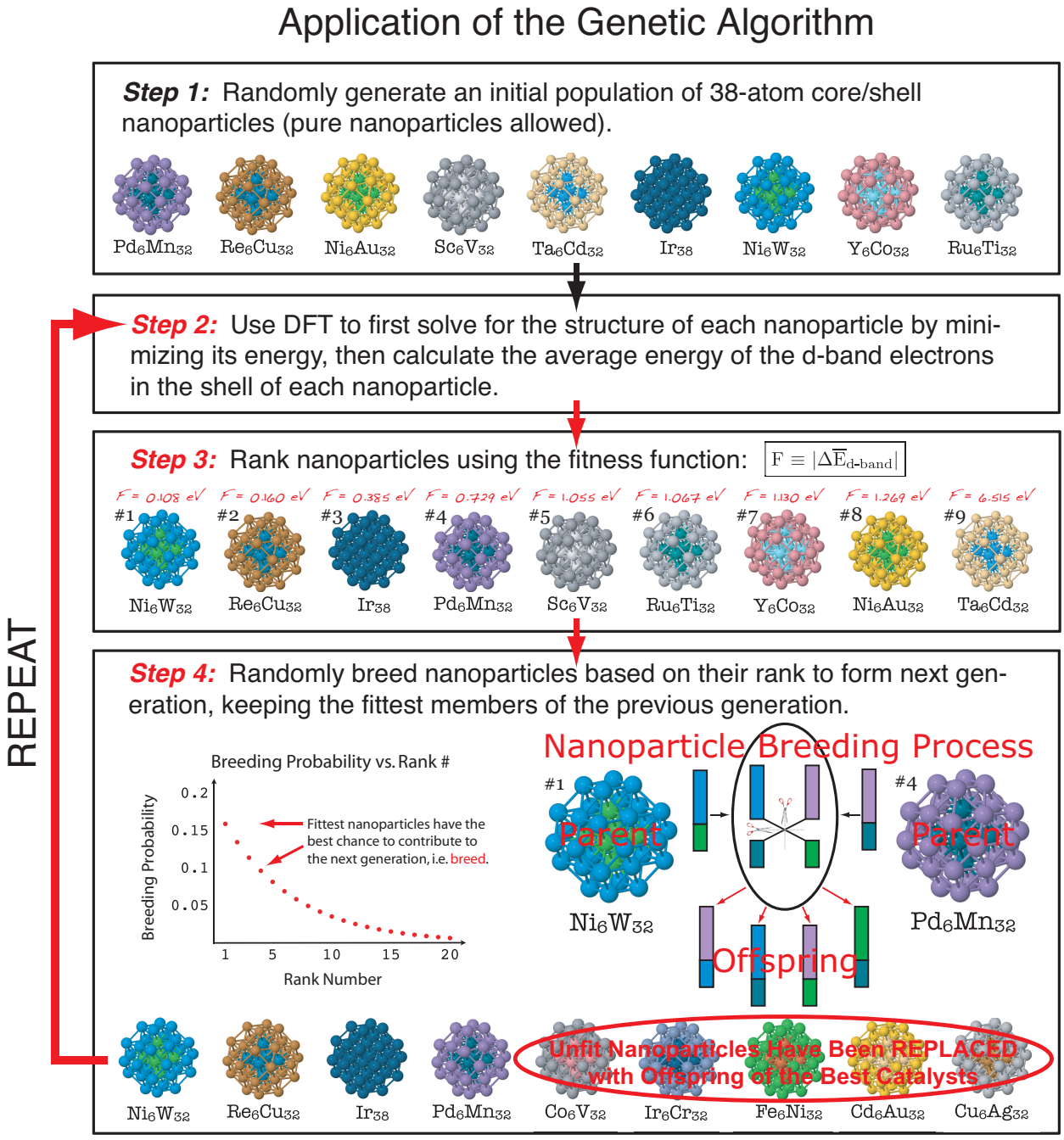

Figure 1.4: Application of the genetic algorithm to 38-atom nanoparticles. See text for discussion.

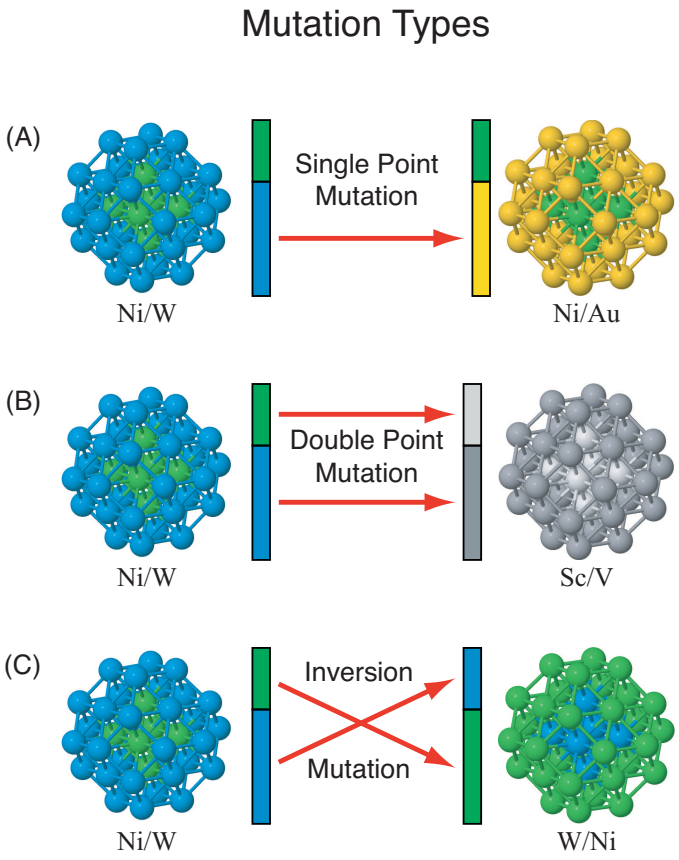

Figure 1.5: Examples of the mutation types that were allowed to occur in the genetic algorithms. Each mutation type occurred with a probability of 10%. (A) Single point mutation, in which one of the metals of the core or the shell is randomly mutated to a new metal. (B) Double point mutation, equivalent to forming a new, entirely random nanoparticle. (C) Inversion mutation, in which the identity of the core and shell metal types is inverted.

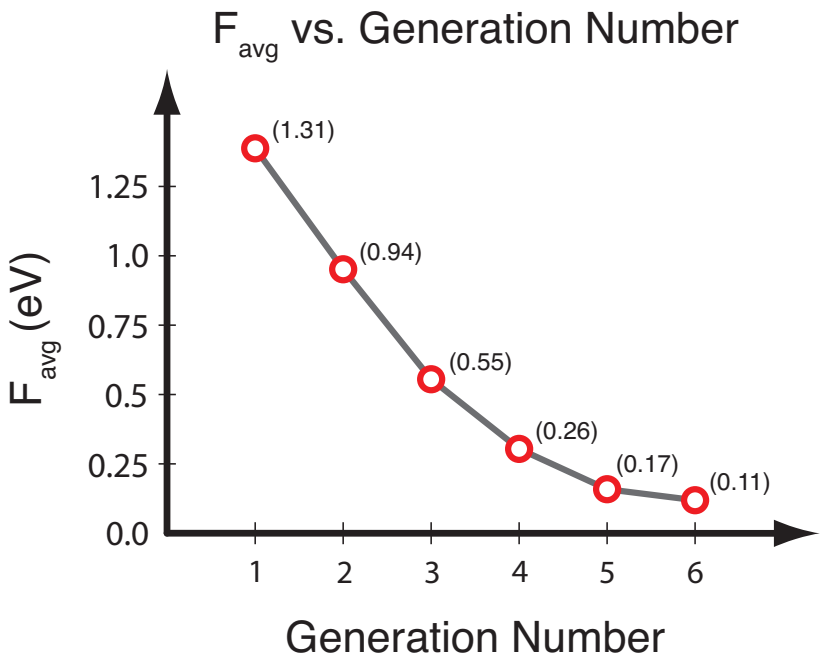

Figure 1.6: Average generation fitness, F_{avg}, plotted as a function of generation number for the 38-atom nanoparticle GA. As can clearly be seen, the generations had essentially converged to optimal fitness after 5-6 generations (indicating that I had properly coded the genetic algorithm). Generation 6 marked the endpoint of the genetic algorithm.

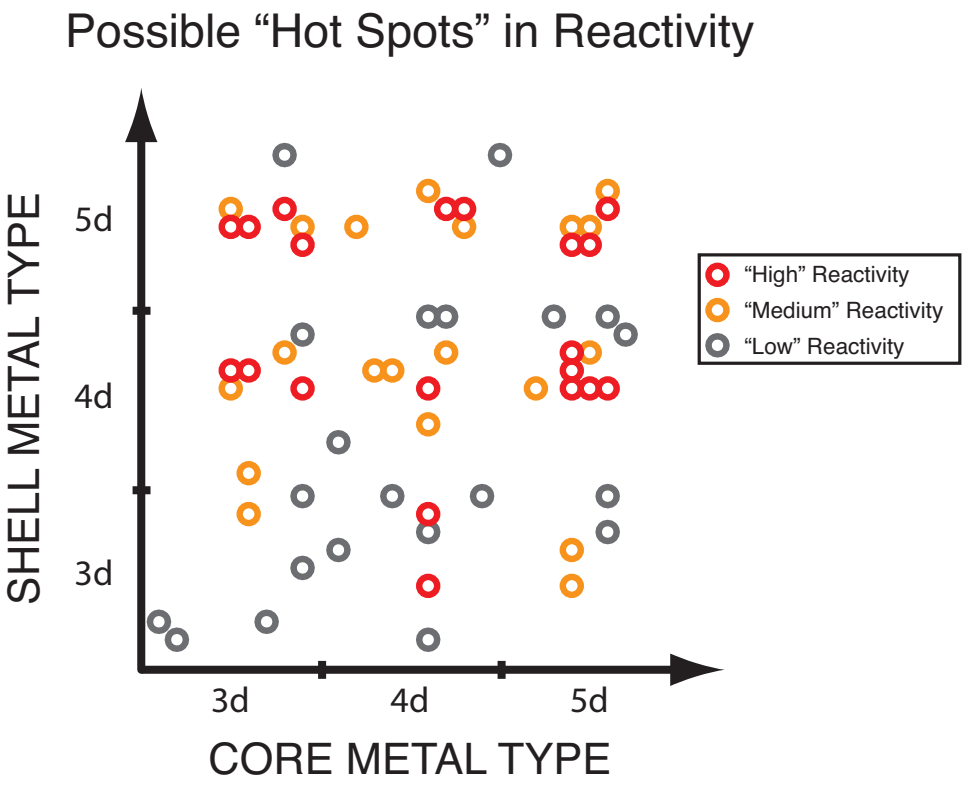

Figure 1.7: Possible "hot spots" in reactivity that might be worth investigating experimentally. As an example, according to the results shown above, it appears that a 5d core (e.g. iridium) with a 4d shell (e.g. silver) might react very similarly to Pt(111) for the oxygen reduction reaction. Quotation marks are used when writing "hot spots" (as well as "high", "medium", and "low" reactivity) because, although these nanoparticles are fit solutions in the genetic algorithm, it remains to be established as to whether the fitness function is actually a good metric for predicting nanoparticle reactivity for the oxygen reduction reaction. (N.B. Not all nanoparticles that turned up in the genetic algorithm are shown above.)

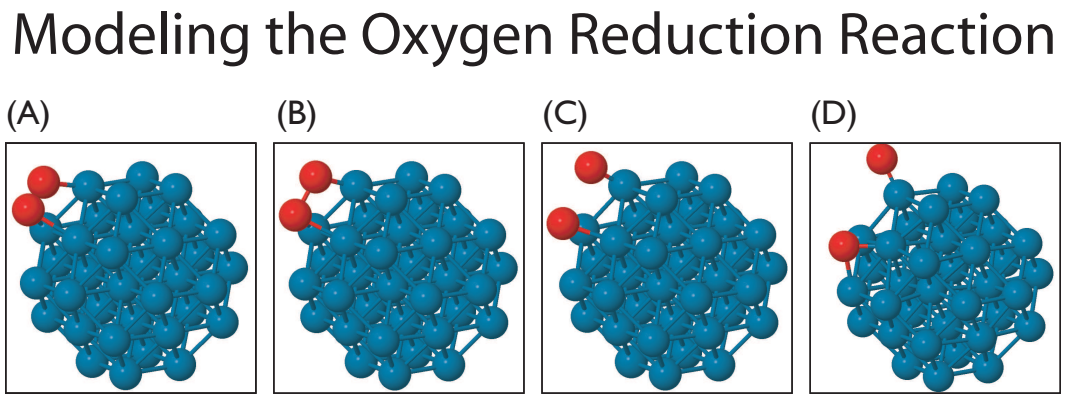

Figure 1.8: O_2 dissociation on a pure 38-atom osmium nanoparticle. This particular nanoparticle was one of the most fit nanoparticles that occurred in the genetic algorithm. However, the reaction shown above actually proceeds *spontaneously*, with the $2O^*$ atoms bonding very strongly (irreversibly) to the osmium nanoparticle. The fact that the reaction is strongly exothermic can be attributed to the *edge atoms* in the nanoparticle's shell. Since the coordination of the edge atoms is low, the d-band is upshifted, and these atoms are more reactive.

Figure 1.8 shows the oxygen reduction reaction occurring on the surface of a pure 38-atom osmium nanoparticles, one of the most fit nanoparticles in the entire genetic algorithm. This particular nanoparticle had an F-value very close to zero, indicating that it might react like Pt(111) for the oxygen reduction reaction. It should be noted that the reaction shown in Figure 1.8 is not *exactly* that of Equation (1.2) since the nanoparticle itself is not charged during the reaction as it would be in the fuel cell. Rather, Figure 1.8 shows the dissociation of O_2,

$$O_2^* \leftrightharpoons [O{\approx}O]^\dagger \leftrightharpoons 2O^*. \tag{1.3}$$

Figure 1.8 helps elucidate a general trend found among the 38-atom nanoparticles for the dissociation of O_2: In general, the *edge atoms* of the nanoparticle were found to be the most reactive atoms on the surface of the nanoparticles. This trend can be rationalized based on coordination number alone – the edge atoms are undercoordinated compared to the central facet atom, and hence, their d-bands are upshifted in energy, leading to heightened reactivity over the central facet atoms. Stated differently, the lower coordination number of the edge atoms translates to less orbital overlap, which in turn translates to less stability of the electrons, and hence the electrons in and edge atom are more inclined to react with the O_2 molecule. Clearly it would have been wise to include *only* the edge atoms in the fitness function, however the main point of the 38-atom nanoparticle GA was to establish a working algorithm; the 79-atom nanoparticle includes a more realistic fitness function.

As mentioned previously, the 79-atom nanoparticle is presently still running. As luck would have it, however, a 79-atom pure osmium nanoparticle happened to turn up in this algorithm. Table 1.1 compares the electronic structures of the 38-atom and 79-atom osmium nanoparticles. As can be

	Core Atoms (eV)	Shell Atoms (eV)	Edge Atoms (eV)	FCC Atoms (eV)
Os_{38}	-6.222	-1.771	-1.750	-2.675
Os_{79}	0.935	-2.095	-1.618	-2.415

Table 1.1: Average d-band energies of different atom types in 38-atom and 79-atom pure osmium nanoparticles. Looking at the core atoms, the average energy of the d-band electrons was *much higher* for the larger nanoparticle. This result seems spurious, although I note that the average energy of the very central atom is -6.013 eV, while the next concentric shell of atoms (i.e. the ones between the very central atom and the shell atoms) is 0.936 eV. Much of the research that remains to be completed will consist of establishing these types of trends. For the shell atoms, the d-band electrons of the larger nanoparticle appear to be more stable (perhaps Os_{79} might not be as reactive as Os_{38} for the ORR as shown in Figure 1.8). For the edge and fcc atoms, the energies of the electrons are very similar (N.B. The shell of Os_{79} contains one atom type that Os_{38} does not. This atom type has apparently downshifted the overall energy of the shell atoms of Os_{79} compared to Os_{38}).

seen in this table, there are some interesting trends. For instance, the d-band energy of the core atoms in Os_{79} are *higher in energy* than those in Os_{38}. This trend is certainly very surprising, although it is noted that the energy of the d-band electrons in the very central atom of Os_{79} is nearly identical to that of the core of Os_{79}. Perhaps the charge density is somehow oscillatory? Much of the remaining research involves understanding the trends involving nanoparticle size, electronegativity, charge transfer, reactivity, etc.

1.5 Conclusion and Future Directions

We have shown that the 38-atom nanoparticle GA rapidly converged to optimal fitness, however, the validity of the fitness function is called into question. It must be remembered that the main goal of the 38-atom nanoparticle GA was to establish a working algorithm (which has involved *a lot* of coding) so that larger, more realistic particles could subsequently be investigated. In this sense, the 38-atom nanoparticle GA has largely been a success. It remains to finish the application of the genetic algorithm to the larger, more realistic 79-atom nanoparticles, to finish investigating how "fit" nanoparticles react for O_2 dissociation, and to establish trends in nanoparticle size, electronegativity, charge transfer, etc. As a result of the trends uncovered in the high reactivities of the 38-atom nanoparticle GA for O_2 dissociation, a different fitness function is being used for the 79-atom nanoparticle GA. It should also be noted that instead of searching for transition states in the reaction $O_2^* \leftrightharpoons [O{\approx}O]^\dagger \leftrightharpoons 2O^*$, only the binding energy of O^* is being investigated in the 79-atom nanoparticle GA since it is thought to be linearly related to the barrier height for O_2 dissociation[3]. The ultimate test, however, will be how the "fit" nanoparticles uncovered by these genetic algorithms react inside *actual* fuel cells. In the very near future I plan on discussing my results with experimentalists (e.g. Dr. Richard M. Crooks and Dr. Keith Stevenson of the Department of Chemistry and Biochemistry) so that the reactivity of fit nanoparticles can truly be assessed. Such a continual feedback loop between experimentalists and theorists is likely the only

way that a problem of this magnitude will actually be solved. It is the hopes that the theoretically based search-and-screen approach outlined above can play some small part in answering the question as to what, if anything, will replace carbon-based fuels as the energy carrier in our future.

Bibliography

[1] C. C. Chusuei, X. Lai, K. Luo, and D. W. Goodman. *Top. Catal.*, 14:71, 2001.

[2] R. W. Scott, O. M. Wilson, and R. M. Crooks. *J. Phys. Chem. B*, 109:692, 2005.

[3] B. Hammer and J. K. Nørskov. Theoretical Surface Science and Catalysis – Calculations and Concepts. *Advances in Catalysis*, 45:71–129, 2000.

[4] P. Hohenberg and W. Kohn. Inhomogeneous electron gas. *Phys. Rev.*, 136(3B), 1964.

[5] W. Kohn and L. J. Sham. Self-consistent equations including exchange and correlation effects. *Phys. Rev.*, 140(4A):A1133–A1138, 1965.

Appendix A

Matehmatical Review

A.1 The Calculus of Variations

The calculus of variations will be used to prove a very important theorem in density functional theory (§B.1), and so we present a brief review of the calculus of variations here. Suppose that we wish to minimize the integral

$$I = \int_{x_1}^{x_2} f(x, y, y')\, dx \ . \tag{A.1}$$

We denote the function that minimizes Equation (A.1) by $y(x)$ and form the one-parameter "trial" functions $\tilde{y}(x)$, defined by

$$\tilde{y}(x) = y(x) + \epsilon\eta(x) \ , \tag{A.2}$$

where $\eta(x)$ is an arbitrary differentiable function for which $\eta(x_1) = \eta(x_2) = 0$ and ϵ is a parameter of that particular family of curves. This ensures that $\tilde{y}(x_1) = y(x_1) = y_1$ and $\tilde{y}(x_2) = y(x_2) = y_2$. Thus the value of the integral (A.1) is now a function of the variable ϵ, and we are concerned with minimizing

$$I(\epsilon) = \int_{x_1}^{x_2} f(x, \tilde{y}, \tilde{y}')\, dx \ , \tag{A.3}$$

meaning that we desire

$$\frac{dI}{d\epsilon} = \int_{x_1}^{x_2} \left(\frac{\partial f}{\partial \tilde{y}} \frac{d\tilde{y}}{d\epsilon} + \frac{\partial f}{\partial \tilde{y}'} \frac{d\tilde{y}'}{d\epsilon} \right) dx \tag{A.4}$$

to be an extremum. From the definition of $\tilde{y}(x)$ in (A.2), the above equation now becomes

$$\frac{dI}{d\epsilon} = \int_{x_1}^{x_2} \left(\frac{\partial f}{\partial \tilde{y}} \eta(x) + \frac{\partial f}{\partial \tilde{y}'} \eta'(x) \right) dx \ . \tag{A.5}$$

Clearly when $\epsilon \to 0$, $\tilde{y} \to y$ and $\tilde{y}' \to y'$, so

$$\left.\frac{dI}{d\epsilon}\right|_{\epsilon=0} = \int_{x_1}^{x_2} \left(\frac{\partial f}{\partial y}\,\eta(x) + \frac{\partial f}{\partial y'}\,\eta'(x) \right) dx = 0 \,. \tag{A.6}$$

Integrating the second term in parenthesis by parts, we obtain

$$\int_{x_1}^{x_2} \frac{\partial f}{\partial y'}\,\eta'(x)\,dx = \left.\frac{\partial f}{\partial y'}\,\eta(x)\right|_{x_1}^{x_2} - \int_{x_1}^{x_2} \frac{d}{dx}\left(\frac{\partial f}{\partial y'}\right)\eta(x)\,dx \,. \tag{A.7}$$

The first term on the left is zero since $\eta(x)$ is zero at x_1 and x_2, leaving us with

$$\left.\frac{dI}{d\epsilon}\right|_{\epsilon=0} = \int_{x_1}^{x_2} \left(\frac{\partial f}{\partial y} - \frac{d}{dx}\frac{\partial f}{\partial y'} \right)\eta(x)\,dx = 0 \,. \tag{A.8}$$

Since $\eta(x)$ is arbitrary but nonzero, the integrand must be equal to zero for the relation to hold, namely

$$\boxed{\left(\frac{\partial f}{\partial y} - \frac{d}{dx}\frac{\partial f}{\partial y'} \right) = 0 \,.} \tag{A.9}$$

This important result is known as the *Euler-Lagrange equation*, which is a necessary condition for the value of the integral in Equation (A.1) to have an extremum value. It should be noted that the symbol δ was used in the early days of the development of the calculus of variations to indicate differentiation with respect to the parameter ϵ. It is analogous to the symbol d in a differential except that it warns you that ϵ and not x is the differentiation variable. Thus the quantity δI (read "the variation of I") is simply the differential

$$\delta I = \frac{dI}{d\epsilon}\,d\epsilon \,, \tag{A.10}$$

where $dI/d\epsilon$ is evaluated for $\epsilon = 0$.

Appendix B

Density Functional Theory

B.1 A Brief Review of Density Functional Theory

In the simple Born-Oppenheimer molecule, the time-independent Hamiltonian for an N-electron system is written as

$$\hat{\mathscr{H}} = T + U + V \tag{B.1}$$

where T is the kinetic energy, U is the potential between the N electrons, and V is the potential due to the external fields, i.e. the nuclear charges. If we let

$$V = \sum_{i=1}^{N} v(\mathbf{r}_i) \ , \tag{B.2}$$

the first Hohenberg-Kohn theorem[4] states that *the potential $v(\mathbf{r})$ is completely determined by the electron density $\rho(\mathbf{r})$ to within an additive constant.* To prove this theorem, we must show that there exists a one-to-one map between $v(\mathbf{r})$ and $\rho(\mathbf{r})$. Assuming a non-degenerate ground state with energy E_0, the Schrödinger equation

$$\hat{\mathscr{H}}\Psi = E_0\Psi \tag{B.3}$$

defines a mapping for each $v(\mathbf{r})$ to the ground state wavefunction Ψ, and from this wavefunction we can find the ground state density $\rho(\mathbf{r})$. It remains to show that two different ground states Ψ and Ψ' arising from different potentials $v(\mathbf{r})$ and $v'(\mathbf{r})$ always give rise to *different* ground state densities. Calling the corresponding Hamiltonians $\hat{\mathscr{H}}$ and $\hat{\mathscr{H}}'$, E_0 is given by

$$\begin{aligned} E_0 = \langle\Psi|\hat{\mathscr{H}}|\Psi\rangle < \langle\Psi'|\hat{\mathscr{H}}|\Psi'\rangle =& \langle\Psi'|\hat{\mathscr{H}}' - V' + V|\Psi'\rangle \\ =& E_0' + \int \rho'(\mathbf{r})[v'(\mathbf{r}) - v(\mathbf{r})]\, d\mathbf{r} \end{aligned} \tag{B.4}$$

Likewise, we can show that

$$E_0' < E_0 - \int \rho(\mathbf{r})[v'(\mathbf{r}) - v(\mathbf{r})]\, d\mathbf{r} \; . \tag{B.5}$$

Adding these two inequalities, we get

$$E_0 + E_0' < E_0' + E_0 + \int [\rho'(\mathbf{r}) - \rho(\mathbf{r})][v'(\mathbf{r}) - v(\mathbf{r})]\, d\mathbf{r} \tag{B.6}$$

By hypothesis, $v'(\mathbf{r})$ and $v(\mathbf{r})$ are different, and so their difference is nonzero. If we assume that $\rho'(\mathbf{r}) = \rho(\mathbf{r})$ we get the self-contradiction

$$E_0 + E_0' < E_0' + E_0 \; . \tag{B.7}$$

Thus, we conclude that the two different densities must correspond to two different potentials, and a non-degenerate ground state can correspond to one and only one potential.

The second Hohenberg-Kohn theorem[5] establishes a variational principle for the energy as a *functional*[1] of the density: *If* $\rho(\mathbf{r})$ *is the density arising from the solution of the* N*-electron Schrödinger equation*

$$\hat{\mathscr{H}}\Psi = E[\rho]\Psi \; , \tag{B.8}$$

then for any density $\rho'(\mathbf{r}) \neq \rho(\mathbf{r})$ *that satisfies*

$$\int \rho(\mathbf{r})\, d\mathbf{r} = N \; , \tag{B.9}$$

we must have $E[\rho'] > E[\rho]$. This theorem follows readily from the one-to-one correspondence between Ψ and $\rho(\mathbf{r})$. By incorporating the N-electron constraint on the density using a Lagrangian multiplier λ, we can formulate the stationary condition at the minimum as

$$\delta\left[E[\rho] - \lambda\left(\int \rho(\mathbf{r})\, d\mathbf{r} - N\right)\right] = 0 \; . \tag{B.10}$$

Substituting for the energy functional in this expression,

$$\begin{aligned} E[\rho] = \langle\Psi|\hat{\mathscr{H}}|\Psi\rangle = \langle\Psi|T+U+V|\Psi\rangle =& \langle\Psi|T+U|\Psi\rangle + \int \rho(\mathbf{r})v(\mathbf{r})\, d\mathbf{r} \\ =& F[\rho] + \int \rho(\mathbf{r})v(\mathbf{r})\, d\mathbf{r} \; , \end{aligned} \tag{B.11}$$

the stationary condition may be re-cast in the Euler-Lagrange form

$$\lambda = \frac{\delta E[\rho]}{\delta\rho(\mathbf{r})} = v(\mathbf{r}) + \frac{\delta F[\rho]}{\delta\rho(\mathbf{r})} \; , \tag{B.12}$$

[1] A functional is function that takes a *function* as its argument and returns a scalar.

where $F[\rho]$ is the universal functional for all systems of N particles with Coulomb interactions. While Equation (B.12) is rather simple in form, it hides the fact that the universal functional $F[\rho]$ is *not* available in explicit form. Numerous schemes have been formulated for a direct optimization of the density based on these stationary conditions. One of the most efficient approach has been to use a quasi-independent-particle approximation as formulated in the Kohn-Sham equations.

To arrive at the Kohn-Sham equations, we assume the existence of a set of orbitals $\{\phi_i(\mathbf{r}),\ i = 1, 2, ..., N\}$ such that the density may be expressed in terms of these orbitals as

$$\rho(\mathbf{r}) = \sum_{i=1}^{N} \phi_i^*(\mathbf{r})\phi_i(\mathbf{r}) \ . \tag{B.13}$$

For a set of non-interacting particles, the term U vanishes and the Hamiltonian becomes

$$\hat{\mathscr{H}} = T + V = \sum_{i=1}^{N} \left(-\frac{1}{2}\nabla_i^2 + v(\mathbf{r}_i) \right) \ . \tag{B.14}$$

The ground state of this system is described by the Slater determinant

$$\Psi = |\phi_1(\mathbf{r}_1)\phi_2(\mathbf{r}_2)\cdots\phi_N(\mathbf{r}_N)| \ , \tag{B.15}$$

where $\{\phi_i(\mathbf{r}_i),\ i = 1, 2, ..., N\}$ are each solutions of the equation

$$\left(-\frac{1}{2}\nabla_i^2 + v(\mathbf{r}_i) \right) \phi_i(\mathbf{r}_i) = \epsilon_i \phi_i(\mathbf{r}_i) \tag{B.16}$$

corresponding to the lowest N eigenvalues.

In a system of interacting electrons, the term U must be included in the Hamiltonian. A large part of this is the Coulomb interaction, and we also expect this to contain some sort of exchange interaction as well as more obscure contributions due to correlation. We define an effective single-particle potential by

$$\int v^{\text{eff}}(\mathbf{r})\rho(\mathbf{r})\, d\mathbf{r} = \int v(\mathbf{r})\rho(\mathbf{r})\, d\mathbf{r} + \frac{1}{2}\iint \frac{\rho(\mathbf{r})\rho(\mathbf{r}')}{|\mathbf{r} - \mathbf{r}'|}\, d\mathbf{r}d\mathbf{r}' + E^{\text{xc}}[\rho] \ . \tag{B.17}$$

The external potential and the direct Coulomb interaction between the charge densities are indicated in the first two terms on the right, while the third term takes care of the exchange and correlation contributions to the interaction potential. Clearly the introduction of particle interactions in the system may also influence the functional form of the kinetic energy term. It is tempting to assume that it remains the same as in the non-interacting case, however this may not necessarily be so. Thus we write the exact kinetic energy functional for the interacting systems as

$$T[\rho] = T^{\text{ni}}[\rho] + \Delta T[\rho] \ , \tag{B.18}$$

where the superscript "ni" denotes that of the non-interacting system and the last term incorporates any changes in the exact kinetic energy functional due to the electron-electron interactions. Collecting all terms, we can express the energy functional for the interacting system as

$$E[\rho] = T^{\mathrm{ni}}[\rho] + \int v(\mathbf{r})\rho(\mathbf{r})\, d\mathbf{r} + \frac{1}{2}\iint \frac{\rho(\mathbf{r})\rho(\mathbf{r}')}{|\mathbf{r}-\mathbf{r}'|}\, d\mathbf{r}d\mathbf{r}' + E^{\mathrm{xc}}[\rho]\ , \tag{B.19}$$

where the correction to the kinetic energy functional has been included in the exchange-correlation functional of the interacting system:

$$E^{\mathrm{xc}}[\rho] = E^{\mathrm{xc,i}}[\rho] + \Delta T[\rho]\ . \tag{B.20}$$

The Euler-Lagrange equation (B.12) now becomes

$$\lambda = \frac{\delta E[\rho]}{\delta\rho(\mathbf{r})} = \frac{T^{\mathrm{ni}}[\rho]}{\delta\rho} + v(\mathbf{r}) + \int \frac{\rho(\mathbf{r}')}{|\mathbf{r}-\mathbf{r}'|}\, d\mathbf{r}' + v^{\mathrm{xc}}(\mathbf{r})\ , \tag{B.21}$$

where the exchange-correlation potential is defined by

$$v^{\mathrm{xc}}(\mathbf{r}) = \frac{\delta E^{\mathrm{xc}}[\rho]}{\delta\rho(\mathbf{r})}\ . \tag{B.22}$$

We note that the last three terms of the Euler-Lagrange equation (B.22) are similar to the effective potential v^{eff} introduced in Equation (B.17) except that now we have included the correction to the kinetic energy functional. We can write the Euler-Lagrange equation as

$$\lambda = \frac{\delta T^{\mathrm{ni}}[\rho]}{\delta\rho(\mathbf{r})} + v^{\mathrm{eff}}(\mathbf{r})\rho(\mathbf{r})\ . \tag{B.23}$$

But the Euler-Lagrange equation for the non-interacting particles was

$$\lambda = \frac{\delta T^{\mathrm{ni}}[\rho]}{\delta\rho(\mathbf{r})} + v(\mathbf{r})\rho(\mathbf{r})\ , \tag{B.24}$$

and this was equivalent to the set of single-particle Schrödinger equations (B.16). By analogy we conclude that for the interacting particles we can find the orbitals from the equations

$$\left(-\frac{1}{2}\nabla^2 + v^{\mathrm{eff}}(\mathbf{r}_i)\right)\phi_i(\mathbf{r}_i) = \epsilon_i\phi_i(\mathbf{r}_i)\ . \tag{B.25}$$

These are known as the *Kohn-Sham equations*, and we note that the density derived from Equation (B.13) automatically fulfills the N-particle constraint, because the orbitals are the orthonormal solutions of an eigenvalue equation.

Optimizing core-shell nanoparticle catalysts with a genetic algorithm

Nathan S. Froemming and Graeme Henkelman[a)]
Department of Chemistry and Biochemistry, The University of Texas at Austin, Austin, Texas 78712-0165, USA

(Received 31 July 2009; accepted 17 November 2009; published online 16 December 2009)

A genetic algorithm is used with density functional theory to investigate the catalytic properties of 38- and 79-atom bimetallic core-shell nanoparticles for the oxygen reduction reaction. Each particle is represented by a two-gene chromosome that identifies its core and shell metals. The fitness of each particle is specified by how close the *d*-band level of the shell is to that of the Pt(111) surface, a catalyst known to be effective for oxygen reduction. The genetic algorithm starts by creating an initial population of random core-shell particles. The fittest particles are then bred and mutated to replace the least-fit particles in the population and form successive generations. The genetic algorithm iteratively refines the population of candidate catalysts more efficiently than Monte Carlo or random sampling, and we demonstrate how the average energy of the surface *d*-band can be tuned to that of Pt(111) by varying the core and shell metals. The binding of oxygen is a more direct measure of catalytic activity and is used to further investigate the fittest particles found by the genetic algorithm. The oxygen binding energy is found to vary linearly with the *d*-band level for particles with the same shell metal, but there is considerable variation in the trend across different shells. Several particles with oxygen binding energies similar to Pt(111) have already been investigated experimentally and found to be active for oxygen reduction. In this work, many other candidates are identified. © *2009 American Institute of Physics*. [doi:10.1063/1.3272274]

I. INTRODUCTION

Platinum-based fuel cells offer an attractive alternative to internal combustion engines as a future means of utilizing chemical energy. There are, however, shortcomings of such technologies that must be resolved if they are to become practical and widespread. Some of these difficulties include CO poisoning, the short lifetime of electrodes in acidic environments, the ~30% energy loss due to slow oxygen reduction kinetics, and the high material cost and limited supply of platinum itself. Cheaper, more effective electrocatalysts need to be developed, yet the task of discovering novel platinum alternatives has proven to be extremely challenging.

Nanoparticles have drawn considerable attention as potential catalysts. One reason is that nanoparticles have high surface-area-to-volume ratios, which could help reduce fuel cell cost since less catalytic material is required. Another reason is that nanoparticles can exhibit strikingly different reactivity than their bulk counterparts. Haruta *et al.*,[1,2] for example, have shown that supported Au particles are very active for low-temperature CO oxidation in the 2–5 nm size range. Bimetallic nanoparticles, moreover, offer the additional prospect of having their reactivity tuned as near-surface alloys.[3,4] Core-shell nanoparticles are excellent candidates because they have well-defined geometries when synthesized in controlled environments, for example, using dendrimer encapsulation techniques.[5,6]

In this work, we identify potential core-shell nanoparticle catalysts for the oxygen reduction reaction (ORR) using a genetic algorithm (GA) to search through the space of possible metal combinations. GAs have been used to solve complex problems in a wide variety of disciplines, including business,[7] bioinformatics,[8–10] chemistry,[11–13] data analysis,[14] economics and finance,[15–18] materials design,[19] and medicine.[20,21] They attempt to optimize an objective (fitness) function using biologically inspired analogs of selection, breeding, and mutation to iteratively refine a population of solution candidates. GAs are especially useful for systems involving discrete variables. In our case, the discreteness in the fitness landscape arises from the elemental identity of the core and shell metals; these are not continuous variables that can be optimized using gradient-based techniques. Our measure of a fit nanoparticle catalyst is that the center of the surface *d*-band is close to that of an effective catalyst, Pt(111). Studies have shown that the *d*-band is a good reactivity descriptor that can be used to predict trends in catalysts with similar geometries and reaction mechanisms.[4,22–24]

In order for GAs to be effective over random or trial-and-error sampling, there must be some structure to the fitness landscape. Two specific requirements are that (i) small mutations of a fit individual will tend to produce other fit individuals, and (ii) the properties that make two individuals fit can be encoded into their genetic information so that cross-breeding them will tend to produce other fit individuals. When these assumptions hold, the GA need only search through a small subset of the entire solution space to find the fittest individuals. We anticipate that the space of bimetallic core-shell nanoparticles is structured so that desirable particle properties can be optimized by a GA, i.e., that varying

[a)]Electronic mail: henkelman@mail.utexas.edu.

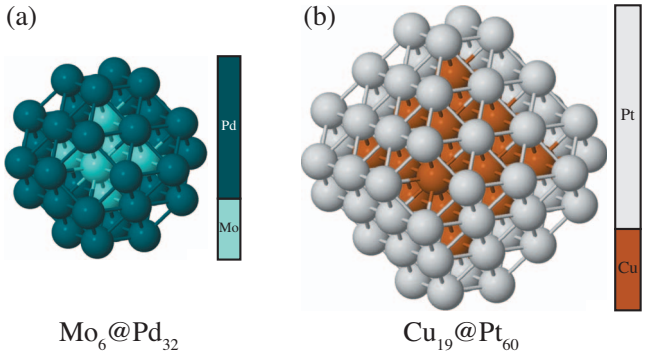

FIG. 1. Examples of the core-shell nanoparticles investigated in this work: (a) a 38-atom particle with a 6-atom molybdenum core and a 32-atom palladium shell, denoted $Mo_6@Pd_{32}$, and (b) a 79-atom $Cu_{19}@Pt_{60}$ particle. To the right of each nanoparticle is its two-gene chromosome.

the core of a particle with a good fitness value will tend to produce other fit particles and that the offspring of two fit particles will also tend to be fit.

II. CALCULATION DETAILS

Density functional theory (DFT) was used in a GA schema to optimize the identity of core and shell metals in 38- and 79-atom nanoparticle catalysts for the ORR. The particles were assumed to have face-centered cubic (fcc) crystal structures with the truncated-octahedral shapes shown in Fig. 1. The 38-atom particles contain a 6-atom core surrounded by a 32-atom monolayer shell, and the 79-atom particles contain a 19-atom core surrounded by a 60-atom monolayer shell. The cores and shells of the particles were taken to be *d*-block metals (viz., the chemical elements in groups 3–12 and periods 4–6 of the periodic table).

A flow chart of the GA used in this work is shown in Fig. 2. In the first step (a) an initial population of 30 core-shell nanoparticles was randomly generated using metals from the *d*-block. Each metal was used once as a core and once as a shell to ensure that a large region of solution space was initially sampled. The particles were given ideal fcc truncated-octahedral crystallite structures (Fig. 1) with the lattice constant chosen as a weighted average of the core and shell bulk fcc lattice constants.[25]

In the second step (b) DFT was used to optimize the structure of each particle in the generation and to calculate the electronic density of states. All DFT calculations were performed with the Vienna *ab initio* simulation package.[26,27] Geometry optimizations were initialized by randomly displacing each atom in the particle by a small amount ($\leq$0.5 Å) to break symmetry. The total energy was then minimized until the force on each atom was less than 0.01 eV/Å. Cubic cells of side lengths 16 and 20 Å contained the 38- and 79-atom nanoparticles, respectively. These cell sizes were chosen so that 8 Å vacuum gap separated the periodic images on average. Electrons in the atomic cores were described using pseudopotentials of the projector augmented-wave framework,[28,29] while valence electrons were described with Kohn-Sham single-electron wave functions[30] expanded in a plane wave basis set up to a kinetic energy cutoff of 300 eV. The exchange-correlation potential was modeled with the

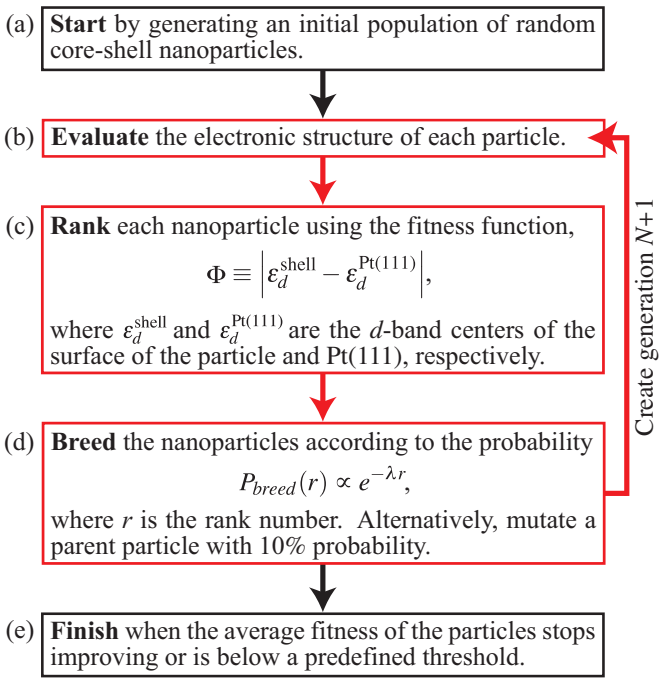

FIG. 2. Overview of the GA (see text for details). The steps in red were repeated to refine the population of candidate nanoparticle catalysts until the stop criterion was met.

generalized gradient approximation using the Perdew–Wang 91 functional.[31] The Brillouin zone was sampled at the Γ-point. Spin polarization was incorporated into all calculations. To accelerate electronic minimization, the occupation of states near the Fermi level was smeared by a width of 0.2 eV using the approach of Methfessel and Paxton.[32] Convergence was checked by increasing the plane wave energy cutoff to 400 eV and increasing the cell volume by 33%; the binding energy of oxygen on Ni_{79} changed by only 11 meV, or less than 0.4%, using these parameters. The symmetry of the particles was monitored during structural optimization. Any particle that did not retain a truncated-octrahedral core-shell geometry was removed from the simulation.

In the third step of the GA [Fig. 2(c)] the fitness of each particle was calculated using the fitness function

$$\Phi \equiv \left|\epsilon_d^{\text{shell}} - \epsilon_d^{\text{Pt(111)}}\right|, \tag{1}$$

where $\epsilon_d^{\text{shell}}$ and $\epsilon_d^{\text{Pt(111)}}$ are the average energies of the *d*-band states in the shell of the particle and at the surface of Pt(111), respectively, each with reference to the Fermi energy.[33] This fitness function aims to quantify the activity of the catalytic surface of the nanoparticle with reference to Pt(111), an effective catalyst for the ORR. Once Φ was computed for all nanoparticles in the generation, the particles were ranked in ascending order of Φ. The particle with the smallest value of Φ received the best rank (r=1), while the particle with the largest value of Φ received the worst rank (r=30, assuming that no nanoparticles were discarded from the generation due to loss of symmetry).

In the fourth step (d) the nanoparticles were bred to produce the next generation. Parent nanoparticles were selected pairwise from the ranked generation according to the probability

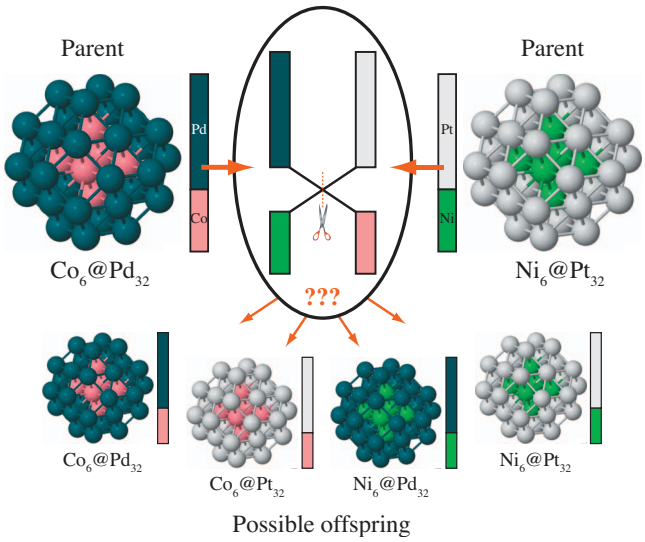

FIG. 3. Two parent particles are bred to produce an offspring particle. Each breeding event led to the formation of a single offspring, chosen at random from the set of possible offspring (in this case, $\{Co,Ni\}_6@\{Pd,Pt\}_{32}$).

$$P_{\text{breed}}(r) = \frac{e^{-\lambda r}}{\sum_{r'=1}^{R} e^{-\lambda r'}}, \tag{2}$$

where $\lambda = \ln 10/(R-1)$ was chosen so that the breeding probability decreased by one decade over the size of the generation, R. The best-ranked particle was therefore 10 times more likely to breed than the worst-ranked particle, yet all particles were allowed to contribute to the next generation. Tests using different values of λ, chosen such that the breeding probability fell off by factors of 5 and 20, and using a step breeding probability function centered about $R/2$ (truncation) changed the number of fit particles found by the GA by less than 4%. This indicates that the performance of the GA is insensitive to the details of the breeding probability.

An example of the nanoparticle breeding process is shown in Fig. 3. A two-gene chromosome was used to identify the core and shell metals of each parent. The chromosomes of the parents were crossed to produce a single offspring nanoparticle for the next generation, chosen at random from the set of possible offspring. The breeding process was repeated until the next generation of 30 nanoparticles was formed. The 79-atom nanoparticles were bred in an identical manner.

Alternatively, parent nanoparticles had a chance to mutate. Mutations introduced randomness into the simulation and prevented the GA from becoming trapped in a local region of solution space. The mutations used in the GA are shown in Fig. 4. In a single-point mutation, either the core or the shell was mutated (with equal probability) to a random transition metal. In a double-point mutation both the core and the shell were mutated, corresponding to the formation of a new, random particle. In an inversion mutation, the core and shell metals were interchanged. The overall probability of a mutation occurring for a parent was 10%; the probability of a particular mutation was 3.3%.

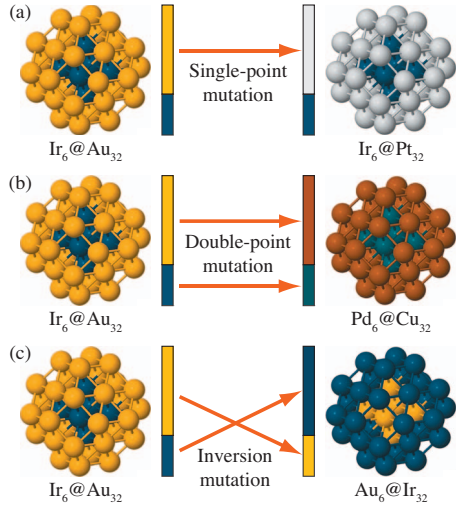

FIG. 4. Mutations used in the GA were (a) single-point, (b) double-point, and (c) inversion. For single-point mutations, either the core or the shell was mutated with equal probability. A mutation occurred with a probability of 10% during each breeding event.

Steps (b)–(d) in the GA were repeated to search for optimal core-shell nanoparticle catalysts. Each generation was evaluated with DFT, ranked, and bred to form the next generation; this generation in turn was evaluated with DFT, ranked and bred to form the next generation, and so on. In this way, the genes of fit particles propagated throughout the generations, and successive generations continually evolved toward optimal fitness. The GA was terminated once the average fitness of the generation dropped below 0.25 eV. Thus, the final generation had catalytic surfaces whose d-band centers were within 0.25 eV of Pt(111).

III. RESULTS AND DISCUSSION

A. 38-atom nanoparticles

Our first GA simulation optimized 38-atom core-shell particles for the ORR. Such particles may be too small to be stable as real catalysts, but they are well suited for testing our methodology. The convergence of the GA is shown in Fig. 5. The GA iteratively refined the population of candidate catalysts until the stop criterion $\Phi_{\text{avg}} \leq 0.25$ eV was reached.

Promising core-shell metal combinations found by the GA are shown in Fig. 6. Horizontal trends are prominent, indicating that the shell metal largely determines the electronic structure at the surface. Good shell metals include Cu, Mo, Os, Pd, Pt, and Ru. The presence of vertical trends in

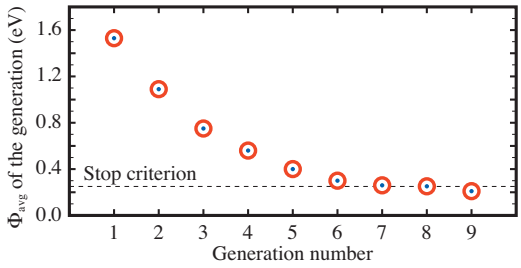

FIG. 5. Convergence of the GA for 38-atom particles. The average fitness of the generation decreased until the stop criterion was met.

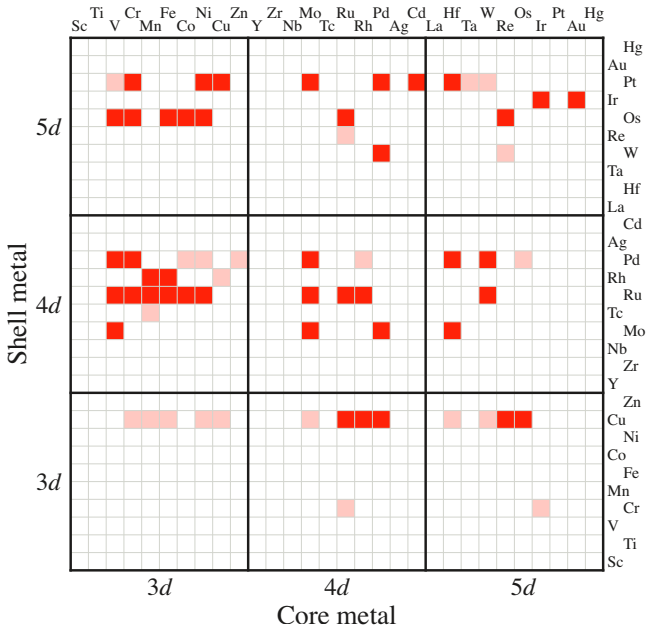

FIG. 6. Promising core-shell metal combinations for 38-atom particles revealed by the GA. Dark squares indicate particles that have $\Phi \leq 0.25$ eV; light squares have $\Phi \leq 0.50$ eV.

Fig. 6 indicates that the core is capable of influencing the electronic properties of the shell. Core metals with small lattice constants such as Cr, Mo, and V stand out. These cores induce compressive strain in the shell and transfer charge to the shell. Both of these effects contribute to a lowering of the surface *d*-band level, which tends to make the shell of the particle more noble.[34] These cores tend to increase catalytic activity by reducing the binding energy of oxygen.

B. Comparison of the GA to other search methods

To compare the effectiveness of the GA to other search methods, we examined all 900 core-shell metal combinations for 38-atom particles and performed a large number of GA, Monte Carlo (MC), and random sampling (RS) simulations. Simulations were run in sets of three so that the initial populations were the same for the methods. Overall, 300 simulations were performed, 100 for each method. Initial populations were chosen as outlined in Sec. II.

Generations of 30 nanoparticles were maintained in the MC and RS simulations; however, the processes by which particles were selected and created for new generations were different from the GA. In the RS simulation, each particle in the population was replaced with a new, random particle. In the MC simulation, a trial particle was generated for each particle in the population by performing a single-point mutation on the original particle (the trial particle therefore either had a different core or a different shell than the original particle; see Fig. 4). Trial particles were passed to the next generation according to the Metropolis acceptance probability[35]

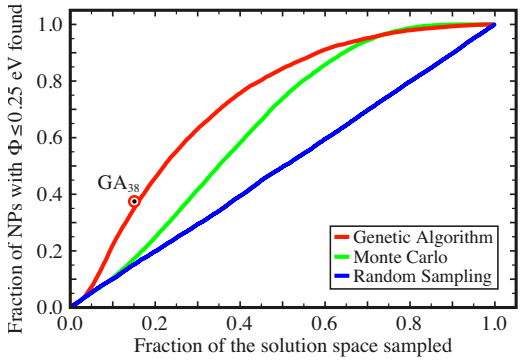

FIG. 7. Comparison of the GA, MC, and RS efficiencies. The fraction of particles with $\Phi \leq 0.25$ eV found is plotted against the fraction of the solution space sampled. The GA in Sec. III A (black dot) found more than twice as many fit particles as the other methods at that fraction of the solution space sampled.

$$P_{\text{accept}} = \min[1, e^{-(\Phi_{\text{new}}-\Phi_{\text{old}})/k_B T}], \tag{3}$$

where $k_B T$ is the effective thermal energy of the sampling, taken to be 0.25 eV, corresponding to an average acceptance probability of 17%.

The different optimization methods are compared in Fig. 7. For RS, the chance of finding a fit particle is constant and equal to their fraction of the solution space. The fraction of fit particles found with RS increases linearly with the fraction of the solution space sampled. Both the GA and MC methods outperform RS. Of the three methods, however, the GA found the fittest particles most efficiently. The GA in Sec. III A (represented by the black dot in Fig. 7) explored 15% of the solution space and found 37% of the fit particles; the MC and RS methods found only 17% and 15% of the fit particles, respectively, at this fraction of the solution space sampled. A comparison of the fit particles found in Sec. III A and the complete set found by brute force is shown in Fig. 8.

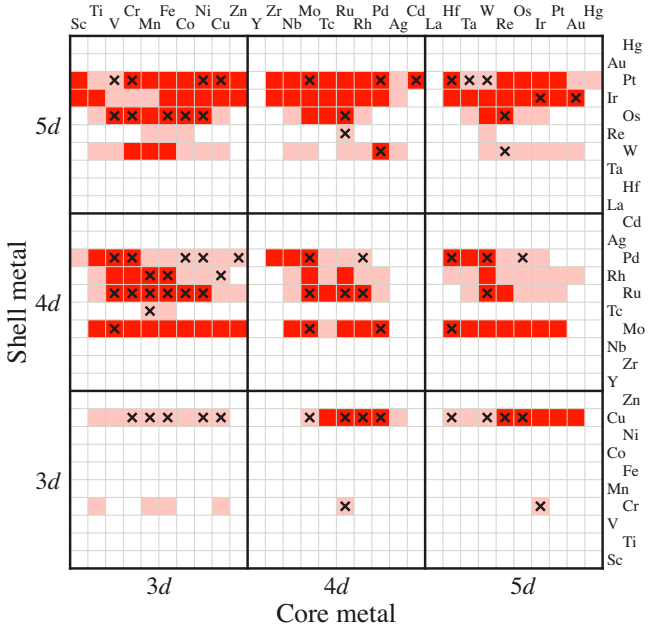

FIG. 8. Best 38-atom nanoparticles out of all 900 possible core-shell combinations. Dark and light squares are defined in Fig. 6. Squares with black X's represent the particles found by the GA in Sec. III A.

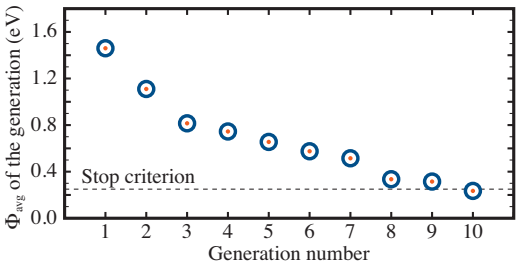

FIG. 9. Convergence of the 79-atom nanoparticle GA.

C. 79-atom nanoparticles

We have also applied the GA to larger, more realistic 79-atom core-shell nanoparticles. The convergence of the GA is shown in Fig. 9. Fit 79-atom particles found by the GA are shown in Fig. 10. Horizontal trends are again prominent, indicating that there may only be a few potential shell metals for use in 79-atom core-shell ORR catalysts. These metals are similar to those found for the 38-atom particles and include Cu, Ir, Os, Pd, Pt, Rh, and Ru.

Stability is an important concern for the small particles. In a few instances, core atoms were found to spontaneously migrate to the shell during structural minimization indicating that the particle was unstable. In the 79-atom GA, 35 of the 176 particles sampled (20%) did not meet our symmetry requirement, and were removed from the GA.

Several of the core-shell metal combinations in Figs. 8 and 10 have been investigated experimentally. Ni@Pt was among the very best of particles found by both the 38- and 79-atom GA. This combination of metals has been shown to be very effective for the ORR by Stamenkovic *et al.*[36] Ru@Pt has been shown by Alayoglu *et al.*[37] to be an effective catalyst for the ORR, as well as for CO oxidation in H_2-rich environments. Other examples include

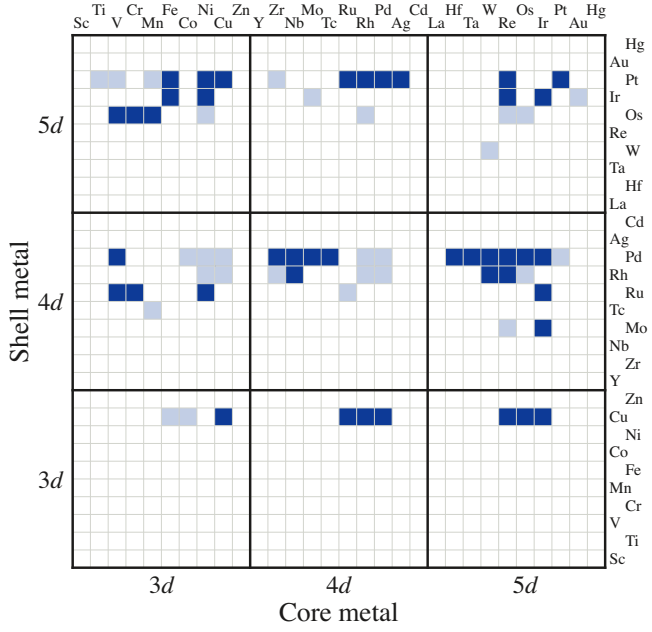

FIG. 10. Promising core-shell metal combinations for 79-atom particles revealed by the GA. Dark and light squares are defined in Fig. 6.

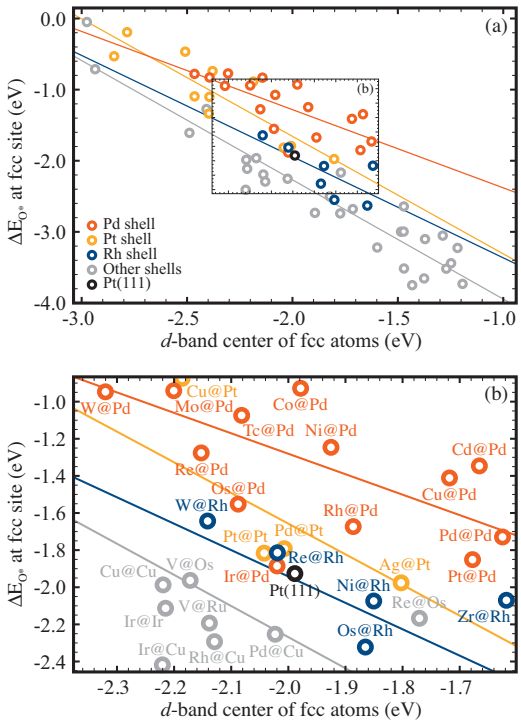

FIG. 11. Binding energy of atomic oxygen at a fcc site vs *d*-band level of the fcc atoms in the shell of 79-atom particles. The inset in (a) is shown in (b) on a larger scale.

Cu@Pt by Koh *et al.*,[38] Fe@Pd by Shao *et al.*,[39] and Co@Pd by Savadogo *et al.*[40] More candidates are shown in Figs. 8 and 10.

D. Oxygen binding on 79-atom particles

The energy level of the *d*-band is a good reactivity descriptor for catalytic activity, but there are other factors that determine adsorbate binding and reaction barriers; these energetics ultimately determine the reaction kinetics.[41,42] To further investigate the fittest 79-atom nanoparticle catalysts, we have calculated the binding energy of atomic oxygen to a fcc site on the (111) facet. The binding energy of oxygen species on transition metals has been shown to be important for the ORR and to correlate well with catalytic activity.[43,44] The (111) facet was chosen because it generally binds adsorbates weakest. Most particles investigated are less noble than Pt and bind oxygen too strongly, so the focus should be on weak binding sites. It is possible, however, that the (100) facet or the edge/corner sites on noble particles have suitable oxygen binding energies to be good catalysts. These sites are not identified here.

The relation between the oxygen binding energy and the *d*-band center is shown in Fig. 11. There is a linear correlation for particles with the same shell metal, yet there is considerable variation in the trend across different shell metals. This behavior is expected since there are other factors that affect adsorbate binding strength, such as the filling of the *d*-band and the overlap between adsorbate and surface metal orbitals. When these factors are constant (a good approximation when the shell metal is the same), a linear trend is observed.

To compare particles with different shell metals, the binding energy of oxygen is a better measure of catalytic activity than the *d*-band level. Metals with somewhat weaker oxygen binding than Pt are expected to have higher ORR activity.[24] An oxygen atom binds at a fcc hollow site on the Pt(111) surface with an energy of 1.93 eV relative to 1/2 O_2(g) at 1/9 monolayer coverage.[33] Binding to the (111) facet of a 79-atom Pt particle is very similar, as can be seen in Fig. 11. In general, the binding energy decreases for reactive cores, e.g., W@Pd, Mo@Pd, and Co@Pd. These trends hold for other common shell metals, e.g., Pt and Rh.

If one knows the active site of the catalyst, the GA can be improved to more specifically target these kinetics. In our case, we used the average *d*-band level of the entire shell in our fitness function. If oxygen binding to a fcc site were known to be a more direct reactivity indicator, however, it would make sense to use the *d*-band level of the fcc atoms or even the oxygen binding energy itself. As long as these indicators are correlated [as in Fig. 11(a)], any one of them may be used to identify an optimal set of candidate catalysts. Subsequent refinements of our fittest nanoparticle catalysts with further calculations and experiments are needed to conclusively identify effective catalysts.

IV. DISCUSSION AND CONCLUSIONS

In this work, we used a GA to find core-shell nanoparticles with *d*-band centers close to that of Pt(111). For 38-atom particles, reactive metals such as V, Cr, and Mo were found to be good cores, while Cu, Ir, Mo, Os, Pd, Pt, Rh, and Ru were found to be good shells. For 79-atom particles, no core metals stood out, and Cu, Ir, Os, Pd, Pt, Rh, and Ru were found to be good shells. Calculations of the oxygen binding energy to the (111) facets of these particles showed a linear correlation with the *d*-band center for particles with the same shell, however, there was significant variation in the trend for different shells. Using the oxygen binding energy as a measure of catalytic activity, we were able to refine the set of fit nanoparticles identified by our GA and suggest new particles that can be tested experimentally.

GAs are only as good as their fitness function(s) allow them to be. In this work, particle fitness was based only on the *d*-band center of the shell, but other properties such as stability and metal cost are also important. Stability is particularly important for core-shell particles whose catalytic properties depend on the specific arrangement of the atoms. Including the surface-segregation energy of the particles in an oxidizing environment, for example, would be a good way to refine our calculations and identify stable particles. The GA could also be extended by using a more detailed genetic encoding, e.g., one that specifies the element identity of every atom in the particle instead of just the core and shell. This would vastly increase the number of candidate catalysts considered and extend their structures beyond the core-shell catalysts considered here. Variable-length chromosomes, moreover, could allow 38-atom particles to breed with 79-atom particles, the offspring of which could contain an intermediate number of atoms.

Promising platinum alternatives must be developed if fuel cells are to replace internal combustion engines as a future means of utilizing chemical energy. Feedback between experimentalists and theorists will likely play a critical role in determining whether such catalysts exist. Optimizing nanoparticles is easier to do computationally than experimentally. Experiments, however, will ultimately determine which catalysts are effective. Subsequent refining of our methods and models will make them more accurate and better able to identify effective catalysts in the future.

ACKNOWLEDGMENTS

This work was supported by the Robert A. Welch Foundation under Grant No. F-160, the Texas Advanced Research Program, and the Department of Energy. N.F. was supported by the Arnold and Mabel Beckman Foundation under the Beckman Scholars Program. We gratefully acknowledge the Texas Advanced Computing Center for computational resources.

[1] M. Haruta, T. Kobayashi, H. Sano, and N. Yamada, Chem. Lett. **2**, 405 (1987).
[2] M. Haruta, N. Yamada, T. Kobayashi, and S. Iijima, J. Catal. **115**, 301 (1989).
[3] F. Besenbacher, I. Chorkendorff, B. S. Clausen, B. Hammer, A. M. Molenbroek, J. K. Nørskov, and I. Stensgaard, Science **279**, 1913 (1998).
[4] J. Greeley and M. Mavrikakis, Nature Mater. **3**, 810 (2004).
[5] R. W. J. Scott, O. M. Wilson, S.-K. Oh, E. A. Kenik, and R. M. Crooks, J. Am. Chem. Soc. **126**, 15583 (2004).
[6] O. M. Wilson, R. W. J. Scott, J. C. Garcia-Martinez, and R. M. Crooks, J. Am. Chem. Soc. **127**, 1015 (2005).
[7] D. Levine, Comput. Oper. Res. **23**, 547 (1996).
[8] *Evolutionary Computation in Bioinformatics*, edited by G. B. Fogel and D. W. Corne (Academic, New York/Elsevier, New York, 2002).
[9] F. H. Van Batenburg and A. P. Gultyaev, J. Theor. Biol. **174**, 269 (1995).
[10] C. Gondro and B. P. Kinghorn, Genet. Mol. Res. **6**, 964 (2007).
[11] D. M. Deaven and K.-M. Ho, Phys. Rev. Lett. **75**, 288 (1995).
[12] M. Damsbo, B. S. Kinnear, M. R. Hartings, P. T. Ruhoff, M. F. Jarrold, and M. A. Ratner, Proc. Natl. Acad. Sci. U.S.A. **101**, 7215 (2004).
[13] P. Willett, Trends Biotechnol. **13**, 516 (1995).
[14] O. Cordón, F. Herrera, and L. Sánchez, in *Genetic Algorithms and Evolution Strategy in Engineering and Computer Science*, edited by D. Quagliarella, J. Périaux, C. Poloni, and G. Winter (Wiley, New York, 1998), pp. 205–224.
[15] M. A. Falcone, H. S. Lopes, and L. D. S. Coelho, Int. J. Comput. Appl. Technol. **31**, 158 (2008).
[16] J. R. Koza, in *Economics and Cognitive Science*, edited by P. Bourgine and B. Walliser (Pergamon, New York, 1991), pp. 57–75.
[17] J.-Y. Potvin, P. Soriano, and M. Vallée, Comput. Oper. Res. **31**, 1033 (2004).
[18] D. Yuret and M. Maza, Technical Analysis of Stocks & Commodities **12**, 58 (1994).
[19] G. H. Jóhannesson, T. Bligaard, A. V. Ruban, H. L. Skriver, K. W. Jacobsen, and J. K. Nørskov, Phys. Rev. Lett. **88**, 255506 (2002).
[20] S. A. Vinterbo and L. Ohno-Machado, Artif. Intell. Med. **18**, 117 (2000).
[21] R. Smigrodzki, B. Goertzel, C. Pennachin, L. Coelho, F. Prosdocimi, and W. D. Parker, Jr., Artif. Intell. Med. **35**, 227 (2005).
[22] J. Greeley, J. K. Nørskov, and M. Mavrikakis, Annu. Rev. Phys. Chem. **53**, 319 (2002).
[23] T. Bligaard, J. K. Nørskov, S. Dahl, J. Matthiesen, C. H. Christensen, and J. Sehested, J. Catal. **224**, 206 (2004).
[24] J. K. Nørskov, J. Rossmeisl, A. Logadottir, L. Lindqvist, J. R. Kitchin, T. Bligaard, and H. Jónsson, J. Phys. Chem. B **108**, 17886 (2004).
[25] Y. Wang, S. Curtarolo, C. Jiang, R. Arroyave, T. Wang, G. Ceder, L.-Q. Chen, and Z.-K. Liu, Calphad: Comput. Coupling Phase Diagrams Thermochem. **28**, 79 (2004).
[26] G. Kresse, Phys. Rev. B **62**, 8295 (2000).
[27] G. Kresse and J. Hafner, Surf. Sci. **459**, 287 (2000).
[28] P. E. Blöchl, Phys. Rev. B **50**, 17953 (1994).

[29] G. Kresse and J. Joubert, Phys. Rev. B **59**, 1758 (1999).
[30] G. Kresse and J. Furthmüller, Comput. Mater. Sci. **6**, 15 (1996).
[31] J. P. Perdew and Y. Wang, Phys. Rev. B **45**, 13244 (1992).
[32] M. Methfessel and A. T. Paxton, Phys. Rev. B **40**, 3616 (1989).
[33] A six-layer $p(3\times3)$ Pt slab was used to calculate the *d*-band level of Pt(111) and the binding energy of O at a fcc site on Pt(111). These calculations used the same DFT parameters as the nanoparticles, except that the Brillouin zone was sampled with a $9\times9\times1$ Monkhorst–Pack *k*-point mesh.
[34] L. Calderín, L. E. González, and D. J. González, J. Chem. Phys. **130**, 194505 (2009).
[35] N. Metropolis, A. W. Rosenbluth, M. N. Rosenbluth, A. H. Teller, and E. Teller, J. Chem. Phys. **21**, 1087 (1953).
[36] V. R. Stamenkovic, B. Fowler, B. S. Mun, G. Wang, P. N. Ross, C. A. Lucas, and N. M. Marković, Science **315**, 493 (2007).
[37] S. Alayoglu, A. U. Nilekar, M. Mavrikakis, and B. Eichhorn, Nature Mater. **7**, 333 (2008).
[38] S. Koh and P. Strasser, J. Am. Chem. Soc. **129**, 12624 (2007).
[39] M. H. Shao, K. Sasaki, and R. Adzic, J. Am. Chem. Soc. **128**, 3526 (2006).
[40] O. Savadogo, K. Lee, K. Oishi, S. Mitsushima, N. Kamiya, and K.-I. Ota, Electrochem. Commun. **6**, 105 (2004).
[41] B. Hammer, L. B. Hansen, and J. K. Nørskov, Phys. Rev. B **59**, 7413 (1999).
[42] B. Hammer and J. K. Nørskov, Adv. Catal. **45**, 71 (2000).
[43] J. K. Nørskov, T. Bligaard, A. Logadottir, S. Bahn, L. B. Hansen, M. Bollinger, H. Bengaard, B. Hammer, Z. Sljivancanin, M. Mavrikakis, Y. Xu, S. Dahl, and C. J. H. Jacobsen, J. Catal. **209**, 275 (2002).
[44] A. U. Nilekar, Y. Yu, J. Zhang, M. B. Vukmirovic, K. Sasaki, R. R. Adzic, and M. Mavrikakis, Top. Catal. **46**, 276 (2007).